Ambipolar Electrochemistry of Pre-Intercalated $Ti_3C_2T_x$ MXene in Ionic Liquid Electrolyte

Geetha Valurouthu,[a] Rachita Panigrahi,[b] Mohit Saraf,[a] Christopher E. Shuck,[a] Bhabani S. Mallik,*[b] Narendra Kurra,*[b] and Yury Gogotsi*[a]

Cation intercalation with or without redox remains the dominant charge storage mechanism for two-dimensional (2D) $Ti_3C_2T_x$ MXene. Anion-based charge storage remains unexplored due to intrinsic negative surface charge of MXenes preventing spontaneous intercalation of anions and irreversible oxidation of Ti at anodic potentials in aqueous electrolytes. In this work, we report on the ambipolar electrochemical behavior of the $Ti_3C_2T_x$ in ionic liquid electrolyte over a 2.5 V electrochemically stable window. The experiments are conducted on a thin $Ti_3C_2T_x$ film current collector coated with an electroactive layer of small flakes (~150 nm) of $Ti_3C_2T_x$ pre-intercalated with 1-ethyl-3-methylimidazolium bis-(trifluoromethylsulfonyl)-imide (EMIM-TFSI) ionic liquid. Couples of redox peaks with a very small potential separation during the voltage sweep are observed at high negative (-0.75 V vs. Ag wire) and high positive ($+0.75$ V vs. Ag wire) potentials. Our experimental electrochemical data combined with density functional theory (DFT) calculations suggest feasibility of pseudo-intercalation of TFSI anions between $Ti_3C_2T_x$ flakes. This study provides a pathway for elucidating anion intercalation for different MXene chemistries in solvent-free electrolytes, which can lead to development of MXene based energy storage devices with improved performance.

Introduction

Understanding the charge storage characteristics at electrochemical interfaces is key to advancing electrochemical energy storage.[1,2] Electrodes made of porous or layered materials encounter various degrees of electrolyte confinement leading to distinctive redox signatures compared to planar interfaces.[3] This nanoconfinement affects solvation dynamics and regulates ion-surface interactions by determining charge storage characteristics.[3,4] MXenes are a class of electronically conductive and redox active two-dimensional (2D) transition metal carbides and/or nitrides that display intriguing charge storage properties depending on the specific electrolyte.[5,6] This family has shown great promise towards high rate pseudocapacitive energy storage in protic electrolytes due to combination of metallic conductivity and rapid (de)protonation of oxygen terminations.[5,7] For instance, $Ti_3C_2T_x$ (where T_x refers to the surface terminations, typically $-OH$, $=O$, $-F$ and/or $-Cl$) shows proton-induced pseudocapacitive behavior, with a volumetric capacitance up to 1500 F/cm^3 in acidic electrolytes, which is about an order of magnitude higher compared to porous carbonaceous materials.[8] The wide compositional versatility, tunable interlayer spacing and surface chemistry make MXenes suitable for designing electrodes of a wide range of energy storage devices such as supercapacitors,[9,10] metal-ion batteries[11] and hybrid metal-ion capacitors.[12]

MXenes are typically synthesized by top-down wet chemical etching of MAX-phase precursors,[5,13] which imparts hydrophilicity and negative charge to the MXene surface, enabling spontaneous intercalation of cations (H_3O^+, Li^+, Na^+, Mg^{+2}, Al^{+3}) from aqueous solutions.[14] However, $Ti_3C_2T_x$ | aqueous electrolyte interfaces are limited by irreversible oxidation at anodic potentials beyond 0.2 V vs. Ag/AgCl in acidic electrolytes.[15] MXene electrodes, therefore, offer stable and reversible electrochemical behavior under cathodic potentials when operated in aqueous electrolytes. Whereas for ambipolar electrochemistry, electrode materials are designed to show reversible electrochemical behavior at both anodic and cathodic potentials.[16] To study the electrochemical behavior of MXenes at positive potentials, non-aqueous electrolytes are used, although the loss of proton-induced pseudocapacitance requires modification of the surface chemistry and electrochemical interfaces to improve the charge storage properties.[17–19] Furthermore, restacking of 2D MXene sheets impedes intercalation and transport of large solvated cations and anions, resulting in poor rate performance in non-aqueous electrolytes.[20] Restacking can be addressed through the design of electrode architectures using spacers such as carbon nanotubes (CNTs),[21] graphene,[22] and pillaring by surfactants.[18] For instance, $Ti_3C_2T_x$/CNT composite electrodes were employed in

[a] G. Valurouthu, Dr. M. Saraf, Dr. C. E. Shuck, Prof. Y. Gogotsi
A. J. Drexel Nanomaterials Institute and Department of Materials Science and Engineering
Drexel University
Philadelphia, PA 19104 (USA)
E-mail: gogotsi@drexel.edu
[b] R. Panigrahi, Dr. B. S. Mallik, Dr. N. Kurra
Department of Chemistry
Indian Institute of Technology Hyderabad
Kandi-502284, Sangareddy, Telangana State (India)
E-mail: bhabani@chy.iith.ac.in
narendra@chy.iith.ac.in

Batteries & Supercaps

Research Article
doi.org/10.1002/batt.202300009

Chemistry Europe
European Chemical
Societies Publishing

organic electrolytes, where CNTs acted as spacers to facilitate the movement of bulky electrolyte ions.[21] However, these large spacers decrease the volumetric capacitance. Alternatively, alkyl ammonium cations pre-intercalated into $Ti_3C_2T_x$ MXene sheets result in enlarged interlayer spacing (2.2 nm) and, when employed with room temperature ionic liquid (IL) electrolytes, deliver high specific capacity with good cycling stability.[20] Recently, Wang et al. demonstrated that the solvent affects the charge storage capacity of MXene electrodes in organic Li-ion containing electrolytes.[23] In an effort to minimize the role of solvent on $Ti_3C_2T_x$ charge storage properties, highly concentrated water-in-salt and solvent-free IL electrolytes were explored. $Ti_3C_2T_x$ electrodes showed an electrochemical anomaly in water-in-salt electrolytes.[24] Shpigel et al. investigated the possibility of anion intercalation into MXene interlayer space by employing concentrated LiCl, LiBr, and 1 M $LiPF_6$/EC/DMC electrolytes[25] and did not find electrochemical insertion of anions into MXene interlayer space within the electrochemically stable window of -0.3 V to 0.5 V (vs. Ag/AgCl).[25] Recently, Tomar et al. reported independent intercalation of cations and anions into a hybrid ($Ti_3C_2T_x$/$LaMnO_{3-\delta}$) nanocomposite material from 3 M KOH electrolyte.[26]

Due to low vapor pressure and solvent-free nature of ILs, MXene|IL interfaces remain electrochemically stable at high anodic potentials (>0.5 V vs. Ag/AgCl).[27] Lin et al. prepared $Ti_3C_2T_x$ ionogel films by vacuum assisted filtration and studied the electrochemical behavior in the neat IL electrolyte.[27] The ion intercalation mechanism from neat IL across MXene interlayer space was probed using in-situ X-ray diffraction.[28] The $Ti_3C_2T_x$ | EMIM-TFSI interface exhibited a typical electric double layer charge storage with redox-like peaks corresponding to cation intercalation.[27] However, the possibility of anion induced redox reactions at MXene | IL interface remains underexplored. Moreover, volumetric changes in the electrodes due to reversible (de)intercalation of bulky ions could impact the mechanical stability and electrical contact with the current collectors. To mitigate this, we used an electrically conductive, compact $Ti_3C_2T_x$ large-flake film for current collectors, while $Ti_3C_2T_x$ small flakes were used to form an ionically conductive layer. $Ti_3C_2T_x$ in IL showed a pair of peaks at about $+0.75$ V vs. Ag wire, besides the peaks in the negative potential window (about -0.75 V vs. Ag wire). This study shows that ambipolar electrochemistry – enhanced cation intercalation and anion pseudo-intercalation may occur in engineered pre-intercalated $Ti_3C_2T_x$ electrodes when the interlayer spacing is made accessible to large ions.

Results and Discussion
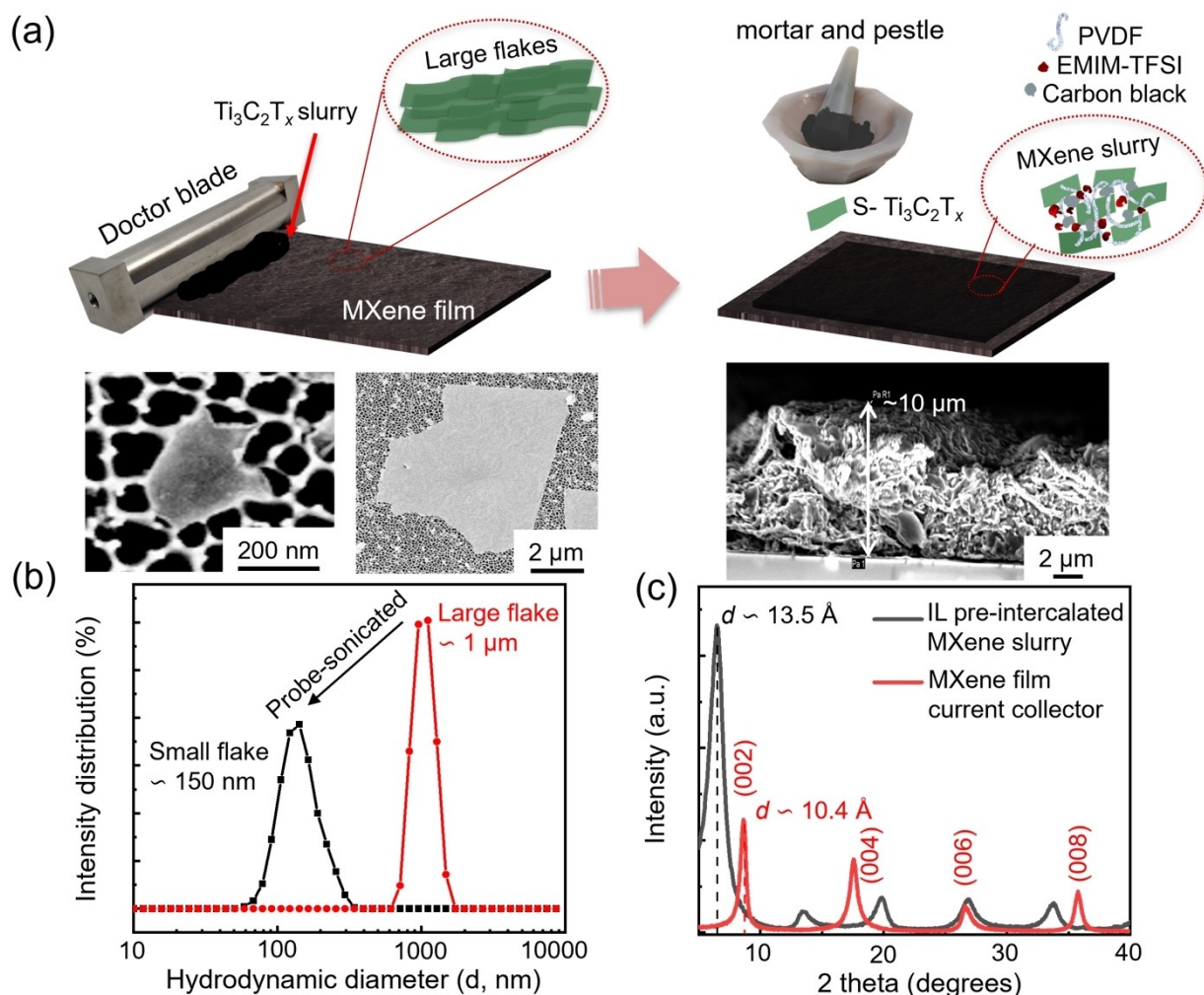
Titanium carbide MXene ($Ti_3C_2T_x$) was synthesized by wet chemical etching and delamination, as described in the Experimental Section.[29] The electrode fabrication process using blade coating method (refer experimental section) is schematically illustrated in Figure 1(a). The $Ti_3C_2T_x$ film with a thickness of 7 μm was blade coated and air dried at room temperature for 12 h followed by vacuum drying at 200 °C for 12 h. It

showed an electrical conductivity of ~15,000 S/cm and was used as a current collector for this study. The high electrical conductivity of the produced free-standing $Ti_3C_2T_x$ films is attributed to good alignment of flakes.[30] The thickness of this current collector is about half of the conventionally used metal foil. Moreover, $Ti_3C_2T_x$ films remain stable at extreme anodic potentials, unlike Al current collectors which corrode under those conditions in presence of TFSI anion.[31] Leveraging its high electrical conductivity and stability at anodic potentials, $Ti_3C_2T_x$ was employed as a current collector and the IL pre-intercalated $Ti_3C_2T_x$ small flakes were cast onto its surface.

Because large-flake films impede ion transport pathways, leading to sluggish ion diffusion kinetics,[32] $Ti_3C_2T_x$ flakes were probe-sonicated to achieve the average flake size of ~150 nm (Figure 1b). However, irrespective of flake size, restacking is a major issue with 2D materials during the film formation because it can hinder electrolyte ion diffusion. Pre-intercalation was found to improve the electrochemical performance of 2D material based electrodes.[33] Previous studies have shown that immersion of free-standing $Ti_3C_2T_x$ films in IL for 72 h lead to intercalation of ions into the interlayer space, improving the electrochemical performance.[27,28] Unlike previous studies, EMIM-TFSI was pre-intercalated via vacuum assisted filtration through the small-flake $Ti_3C_2T_x$ wet filtrate cake during film formation to reduce restacking. Additionally, conventional electrode slurry preparation (refer Experimental Section) was utilized to further improve the ionic accessibility between the $Ti_3C_2T_x$ layers, where carbon black was introduced as a spacer to support the easy movement of large cations through the $Ti_3C_2T_x$ electrode, while binder was added for improving adhesion of the active layer to the MXene current collector. This strategy of using thin and compact $Ti_3C_2T_x$ films as current collectors providing fast electronic transport and pre-intercalated low-density MXene slurry as an electroactive layer with a fast ionic transport is useful when working with organic and IL electrolytes with large cations and anions.

The structure of the $Ti_3C_2T_x$ electrodes was characterized by X-ray diffraction (XRD), as shown in Figure 1(c). The $Ti_3C_2T_x$ current collector showed prominent (00l) peaks with (002) at 7.2° (d-spacing of 10.4 Å; thickness of $Ti_3C_2T_x$ flake is 9.4 Å). The slurry coated $Ti_3C_2T_x$ film showed (002) peak at 6.2° (d-spacing of 13.5 Å; interlayer space of ~4.1 Å), suggesting the enlarged interlayer spacing of MXene layers is due to pre-intercalated electrolyte ions. We noticed an increase in d-spacing from 10.4 Å to 12.9 Å by soaking the MXene film in ionic liquid electrolyte (Figure S1). This observation agrees with our earlier work and is attributed to the spontaneous ion intercalation into $Ti_3C_2T_x$ MXene on contact with EMIM-TFSI.[34] Typical sizes of EMIM (7.74 Å × 4.21 Å) and TFSI (7.44 Å × 4.41 Å) ions are <1 nm, possibly reducing the energy barriers for diffusion in the case of pre-intercalated electrodes. The full width at half maximum (FWHM) of (002) peak of the IL pre-intercalated MXene slurry casted electrode is larger than the $Ti_3C_2T_x$ current collector film and the ionic liquid soaked film (Figure S1), indicating a less ordered stacking (due to smaller flake size and differing amounts of intercalant between the flakes). Cross-sectional SEM image of the IL pre-intercalated $Ti_3C_2T_x$ coating

Batteries & Supercaps

Research Article
doi.org/10.1002/batt.202300009

Chemistry Europe
European Chemical
Societies Publishing

Figure 1. a) Schematic representation of slurry coating of EMIM-TFSI pre-intercalated $Ti_3C_2T_x$ small flakes (~150 nm) mixed with carbon black and PVDF binder on $Ti_3C_2T_x$ MXene films prepared by doctor blade coating of larger flakes (~1 μm). b) Dynamic light scattering of small (~150 nm) and large flakes (~1 μm), with their representative SEM micrographs. c) X-ray diffraction patterns of $Ti_3C_2T_x$ current collector (red profile) and ionically conductive layer (IL pre-intercalated $Ti_3C_2T_x$ slurry coating, grey profile). Cross-sectional SEM image of ionically conductive MXene layer.

(top inset of Figure 1c) shows a more open structure with random orientation of flakes which is consistent with XRD data.

The electrochemical performance of the pristine and pre-intercalated $Ti_3C_2T_x$ electrodes was investigated in pure EMIM-TFSI (IL) and 1 M EMIM-TFSI in PC solvent. Neat IL refers to EMIM-TFSI without a solvent added. As shown in Figure 2(a), cyclic voltammetry curves (CVs) of pre-intercalated $Ti_3C_2T_x$ | EMIM-TFSI, pristine $Ti_3C_2T_x$ | EMIM-TFSI, and pre-intercalated $Ti_3C_2T_x$ | 1 M EMIM-TFSI:PC interfaces showed similar signatures with a prominent pair of peaks at −0.75 V (vs. Ag wire) and 0.75 V (vs. Ag wire) on top of rectangular capacitive envelops (Figure S2, Supporting Information). Based on previous in-situ XRD measurements, the peaks at negative potentials (−0.75 V vs. Ag wire) are assigned to intercalation of EMIM cations with an expansion of interlayer spacing.[28] However, the origin of the peaks around 0.75 V (vs. Ag wire) is not clear and may be due to cation deintercalation or anion intercalation under anodic potentials.

To rule out contributions from external glassy carbon current collectors and carbon black in the $Ti_3C_2T_x$ electrodes, control experiments were carried out. None contribute to the peaks at the extreme anodic potentials, meaning that those peaks originate solely from $Ti_3C_2T_x$ charge host (Figure S3, Supporting Information). The prominent pairs of reversible peaks between −1.5 V and 1.0 V can be attributed to intercalation/deintercalation of $EMIM^+/TFSI^-$ ions from ionically conductive MXene electrodes as there is no solvent used. In our earlier study, the electrostatic attraction between intercalated $TFSI^-$ anions and positively charged MXene layers and/or steric effect originating from de-intercalation of EMI^+ cations was shown to lead to a decrease of the interlayer spacing in MXene under positive polarization.[28] Further in-situ electrochemical characterization will be required to determine the origin of the peaks in pre-intercalated films used in our study. It was proposed that in an electrolyte confined microenvironment, the charge-storage mechanism can be a continuum between double-layer and redox charge storage.[3] Because the
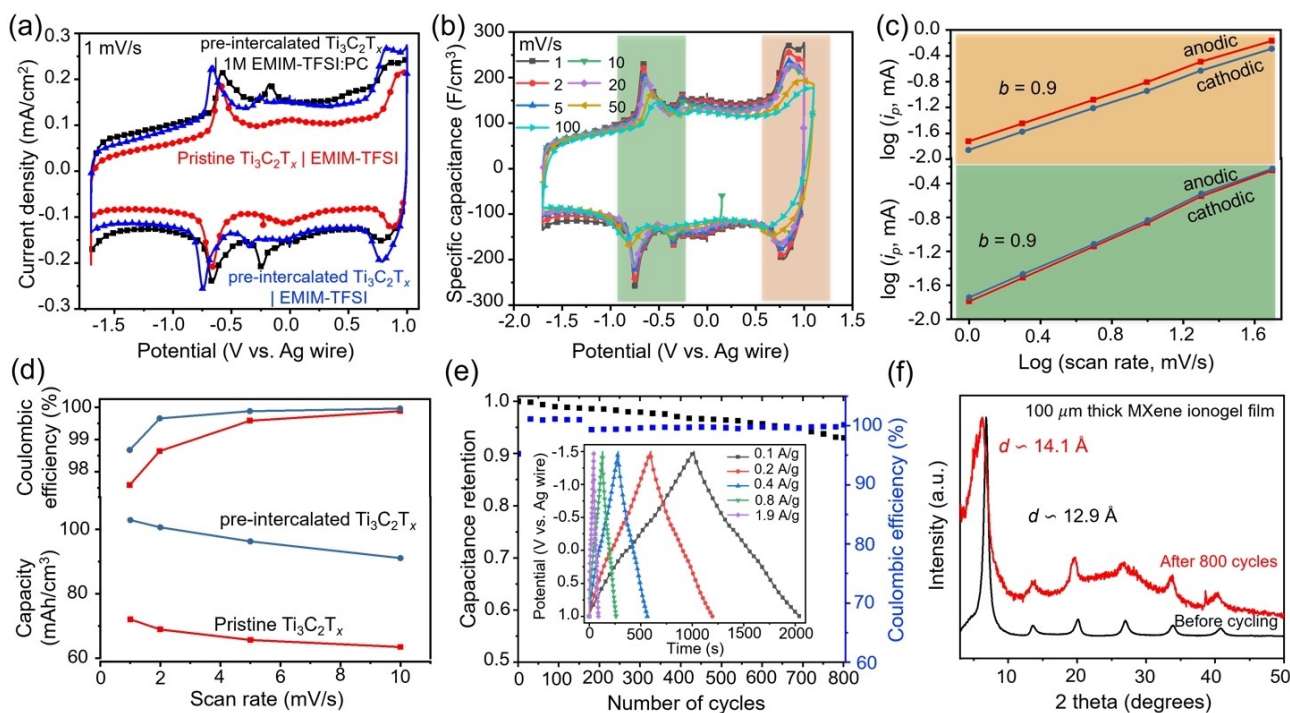
Figure 2. a) Cyclic voltammograms of $Ti_3C_2T_x$ electrodes with and without pre-intercalation tested in pure EMIM-TFSI and 1 M EMIM-TFSI in PC electrolytes at a scan rate of 1 mV/s. b) CVs of pre-intercalated $Ti_3C_2T_x$ electrodes from 1 to 100 mV/s scan rates in pure EMIM-TFSI electrolyte. Prominent peaks in the negative and positive potential windows are marked. c) Variation of log (peak current) versus log (scan rate), slope corresponds to a "b" value of 0.9. d) Capacity and Coulombic efficiency of $Ti_3C_2T_x$ electrodes (pre-intercalated and pristine) as a function of scan rate. e) Cycling stability of the pre-intercalated MXene electrodes for 800 cycles at a scan rate of 10 mV/s; representative charge-discharge profiles at different current densities (0.1–1.9 A/g) are shown in the inset. f) Ex-situ XRD patterns showing the expansion of interlayer spacing ($\sim$1.2 Å c lattice parameter) after electrochemical cycling.

$Ti_3C_2T_x$ | electrolyte interface is not planar (top inset of Figure 1c), charge/discharge may occur continuously with changing potential, leading to pseudocapacitive charge storage.

Among the three couples studied, pre-intercalated $Ti_3C_2T_x$ in EMIM-TFSI showed the maximum total capacitance and presence of two pairs of peaks. Specific capacitance is a measure of the charge stored per unit voltage in an electrode per unit area or unit mass or unit volume. Figure 2(b) shows specific capacitance (F/cm^3) plotted against the potential (V vs. Ag wire) from CVs recorded at scan rates from 1 to 100 mV/s, had a rectangular box profile with overlayed peaks. The peak-to-peak separation was less than 100 mV until scan rate of 10 mV/s, indicating fairly reversible electrochemical behavior. To further understand the electrochemical kinetics, log (peak current) versus log (scan rate) was plotted for both pairs of redox peaks. The slope of log i_p vs. log (scan rate) gives an estimate of 'b', which determines the rate limiting step of electrochemical reactions. When 'b' is unity, it corresponds to a capacitive process (surface controlled) while 0.5 corresponds to a diffusion limited process. In this case, b is 0.9, signifying a predominantly capacitive process with minor contributions from diffusion (Figure 2c).[35,36]

Pre-intercalated $Ti_3C_2T_x$ electrodes showed better charge storage capacity and Coulombic efficiency than pristine $Ti_3C_2T_x$ as shown in Figure 2(d). We observed nearly 40% gain in the charge storage capacity with a Coulombic efficiency above

99% for pre-intercalated $Ti_3C_2T_x$, which can be attributed to accessible to ions in the MXene interlayer space. At a mass loading of 2.0 mg/cm^2, the pre-intercalated $Ti_3C_2T_x$ showed a typical specific capacity of 48 mAh/g (corresponding volumetric capacitance of 140 F/cm^3) at 5 mV/s. The integrated value of specific capacitance corresponds to 64 F/g in the voltage window of 2.7 V. The typical rate performance is 90% when the scan rate was increased from 1 to 10 mV/s. When the same electrodes were tested in sulfuric acid, which provided small and fast protons, the specific capacity was $\sim$60 mAh/g, which is about 20% higher compared to the IL electrolyte (Figure S4, Supporting Information). The charge storage capacity of the electrodes is dependent on many factors such as electrode architecture, electrolyte wettability, and size of the charge storage ions.[4] Though there is a large size difference between the ions of protic electrolyte (H^+) and IL ($EMIM^+$/$TFSI^-$), no large difference in the amount of charge stored was observed for pre-intercalated $Ti_3C_2T_x$, which demonstrates the open electrode architecture. Further, the electrochemical stability of the electrode was investigated for 800 cycles at 10 mV/s, showing a capacity retention of $\sim$95% while maintaining a Coulombic efficiency of $\sim$99% (Figure 2e). Ex-situ XRD was performed on the electrodes after 800 electrochemical cycles to confirm the lack of phase change upon intercalation of EMIM and TFSI ions (Figure 2f). The (002) peak shifted to lower 2θ (6.52°), demonstrating a slightly expanded d-spacing (1.2 Å). We observed a similar volumetric change of up to 10% which

Batteries & Supercaps

Research Article
doi.org/10.1002/batt.202300009

**Chemistry
Europe**

European Chemical
Societies Publishing

was previously reported in the case of $Ti_3C_2T_x$ electrodes in the IL electrolyte.[37]

Electrochemical impedance technique provides information about the reaction kinetics, diffusion processes, and capacitive behavior as a function of frequency.[38] Figure 3(a) shows a Nyquist plot at different potentials and the nature of the plots varies depending on the potential applied to the working electrode. Inset shows high frequency semicircles with diameter varying with respect to the potential. This variation can be attributed to the charge transfer resistance at the $Ti_3C_2T_x$ | IL interface. It is observed that the radius of the semicircle gradually increases by imposing the anodic potentials. The resistance corresponding to the mid frequency region increases from $2.75\ \Omega\,cm^2$ to $3\ \Omega\,cm^2$ by changing the potential of the working electrode from 0 to 1 V (vs. Ag wire). $Ti_3C_2T_x$ surface is positively charged and could attract $TFSI^-$ ions by electrostatic interactions. But it is not clear which surface site (either −O or a defect) accommodates $TFSI^-$ ions with subsequent charge transfer. In the case of cation intercalation across MXene interlayer space, the mechanism is relatively well established. Intercalation of anions has been less explored and no conclusion about its possibility can be drawn until this point. Again, the kinetic parameter "b" turns out to be 0.9 for the peaks at negative and positive potentials. While the cation deintercalation and anion attraction are possible options,

assuming anion intercalation occurring, a higher charge transfer resistance at anodic potentials (1 V vs. Ag wire) can be explained by an energy barrier associated with the anionic redox process due to repulsive interactions between the negatively charged $Ti_3C_2T_x$ and anionic charge species.[25] The high-frequency X-axis intercept corresponds to the equivalent series resistance (ESR) of the electrochemical cell. Independent of the potential on the $Ti_3C_2T_x$ electrode, the ESR value was found to be $1.33\ \Omega\,cm^2$.

To understand the ionic diffusion behavior across $Ti_3C_2T_x$ galleries, the real part of the impedance (Z') is plotted against $\omega^{-1/2}$, by choosing frequencies corresponding to the Warburg region.[39] Warburg coefficient (σ) is estimated from the slope of Z' vs. $\omega^{-1/2}$ ($Z' = \sigma\,\omega^{-1/2}$) and is inversely proportional to the diffusion coefficient ($D \sim \sigma^{-2}$).[40] The Warburg coefficient is higher ($76\ \Omega\ s^{-1/2}$) at anodic potentials compared to cathodic potentials ($45\ \Omega\ s^{-1/2}$) (Figure 3b). The relative ratio of $TFSI^-$ to $EMIM^+$ diffusion coefficients in the $Ti_3C_2T_x$ interlayer space is estimated to be 0.35. Therefore, the relatively sluggish diffusion kinetics of $TFSI^-$ across $Ti_3C_2T_x$ interlayer space compared to $EMIM^+$ could be attributed to the repulsive interactions between the anions and negative surface charge of $Ti_3C_2T_x$. To map out the charge storage dynamics, 3D Bode maps were constructed in the capacitive frequency domain (10 mHz to 10 Hz). As shown in Figure 3(c), protruded regions at specific
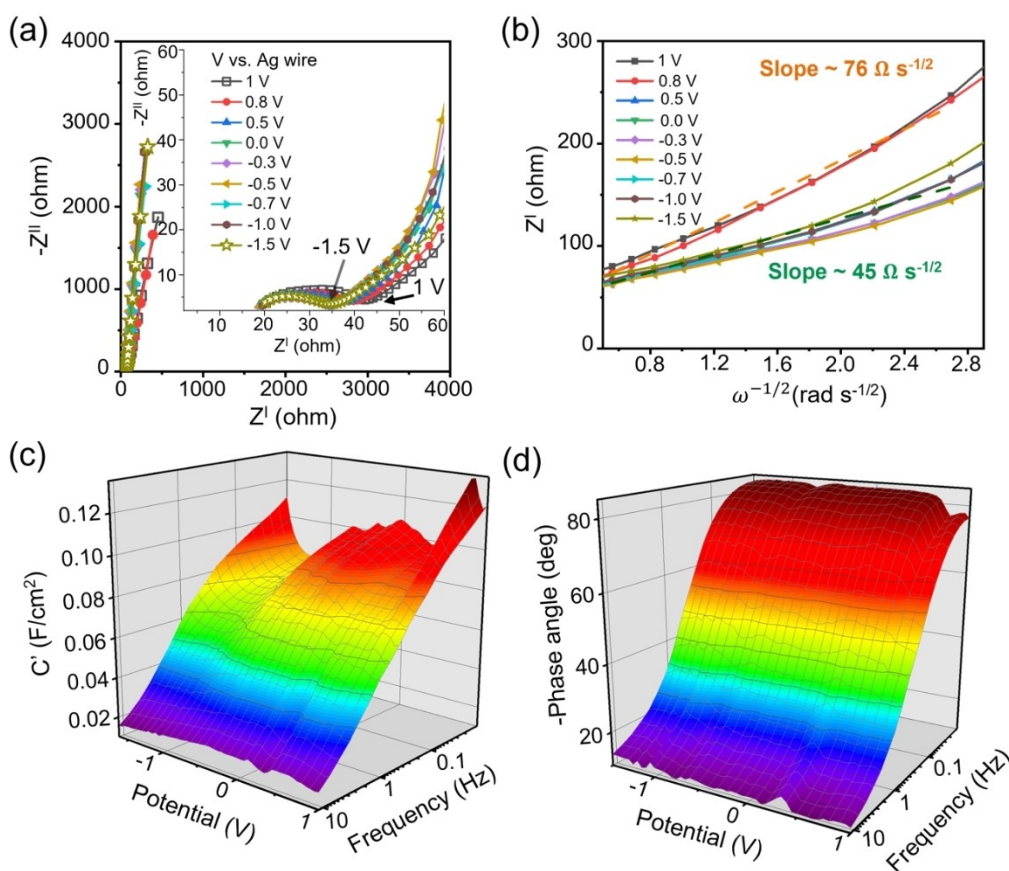
Figure 3. a) Nyquist plots at different potentials; the inset shows the high frequency region with a semicircle and the 45° line. b) Real impedance versus $\omega^{-1/2}$ at different potentials to estimate Warburg coefficients from the slope values. 3D Bode maps of c) real areal capacitance-potential-frequency and d) phase angle-potential-frequency of pre-intercalated $Ti_3C_2T_x$ | neat EMIM-TFSI couple.
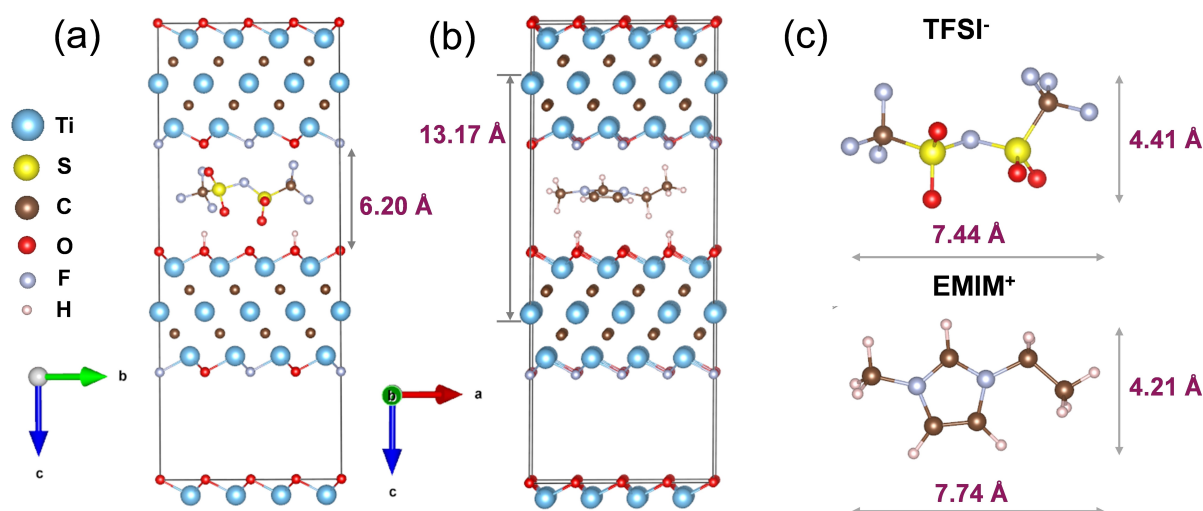
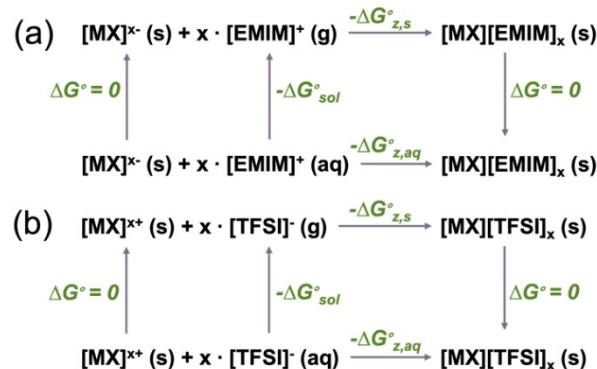**Figure 4.** Schematic representation of the optimized confirmation of the ions intercalated into $Ti_3C_2T_x$ interlayer space from DFT calculations; arrangement of the intercalated ions a) TFSI$^-$ and b) EMIM$^+$ between the MXene sheets. c) The bare ionic sizes of isolated cationic and anionic species.

potentials in the low-frequency 3D Bode capacitance plot correspond to EMIM$^+$ and TFSI$^-$ intercalation/deintercalation at about -0.75 V and 0.75 V (vs. Ag wire), respectively. In contrast, dips in the 3D phase angle maps (Figure 3d) were observed at the same potentials as the intercalation, because redox reactions are slower than the ion adsorption (double-layer formation).

To further understand the feasibility of EMIM$^+$ and TFSI$^-$ intercalation, DFT calculations were performed. A $4\times4\times1$ supercell of $Ti_3C_2T_x$ with a stoichiometry of $Ti_3C_2O_{0.84}F_{0.25}(OH)_{0.06}$ (abbreviated as MX) was chosen as it was the closest to the experimental stoichiometry (refer to Experimental Section).[25] The most energetically favorable arrangement of terminations on the MXene surface was considered by following a previous report.[25] The most favorable conformation of the intercalated ions is illustrated in Figure 4. The intercalation energetics of TFSI$^-$ and EMIM$^+$ (corresponding conformations are shown in Figure 4(a) and (b), respectively) into the positively and negatively charged $Ti_3C_2T_x$ can be investigated by calculating the intercalation free energy values. The ionic sizes of bare TFSI$^-$ and EMIM$^+$ ions are depicted in Figure 4(c). The adopted intercalation mechanism for DFT calculations can be represented using the thermodynamic cycle as shown in Figure 5.[25]

Here, $\triangle G^0_{z,s}$ and $\triangle G^0_{z,aq}$ are the free energies corresponding to the intercalation of gas-phase ions, and aqueous ions, respectively; $\triangle G^0_{sol}$ is the solvation free energy of the intercalating ions; and x is the number of ions intercalated into the MXene sheets to maintain the charge neutrality. $\triangle G^0_{z,aq}$ for cations and anions were calculated using Equations (1) and (2):

$$\Delta G^0_{z,aq}\,[\text{EMIM}]^+ = \Delta G^0_{z,s} - \Delta G^0_{sol}$$

$$= E\,[\text{MX-EMIM}] - E\,[\text{MX}]^{x-} - x\cdot E\,[\text{EMIM}_{(g)}]^+$$

$$-x\cdot\Delta G^0_{sol}\,[\text{EMIM}]^+$$

$$= -14.56\text{ eV} \qquad (1)$$

Figure 5. Thermodynamic cycle adopted to calculate the free energy values of a) EMIM$^+$ and b) TFSI$^-$ ions intercalation in the MXene interlayer space.

$$\Delta G^0_{z,aq}\,[\text{TFSI}]^- = \Delta G^0_{z,s} - \Delta G^0_{sol}$$

$$= E\,[\text{MX-TFSI}] - E\,[\text{MX}]^{x+} - x\cdot E\,[\text{TFSI}_{(g)}]^-$$

$$-x\cdot\Delta G^0_{sol}\,[\text{TFSI}]^-$$

$$= +6.91\text{ eV} \qquad (2)$$

The solvation energy of TFSI$^-$ and EMIM$^+$ in the implicit solvent was calculated using the VASPsol software package[41,42] assuming that $\triangle G^0_{z,s}$ can be approximated to an intercalation electronic energy. $E[\text{M}]$ in the above equations is the calculated electronic energy for a system $[\text{M}]$.

The electronic energies for all the charged systems are reported in Table S1, Supporting Information. The calculated intercalation free energy in the solvation sheath for EMIM$^+$ is -14.5 eV. As expected, the cation intercalation into the MXene interlayer space is a thermodynamically favorable process, which is in line with CV observations where redox peaks were observed at approximately -0.75 V (vs. Ag wire). Different conformations of EMIM$^+$ in the intercalated state were considered, as shown in Figure S5, Supporting Information.

Batteries & Supercaps

Research Article
doi.org/10.1002/batt.202300009

Chemistry
Europe

European Chemical
Societies Publishing

Based on DFT calculations, the $EMIM^+$ prefers a parallel orientation with the surface of the MXene sheet. On contrary, intercalation free energy of $TFSI^-$ in the solvation shell is 6.9 eV, which is thermodynamically unfavorable. This agrees well with the previous reports that the intercalation of the solvated anions (Cl^-) into the MXene sheets is unfavorable due to the electrostatic repulsion between intercalating anions and the host MXene lattice.[25]

Under the open circuit voltage (OCV), anions usually experience expulsion effect due to negative surface charge of MXenes.[25] However, in the desolvated phase, the free intercalation energies of neat $EMIM^+$ and $TFSI^-$ species were reduced by 1.5 and 1.1 eV, respectively, in comparison to the solvated state (Table S2, Supporting Information). Though anion intercalation energy in both, the desolvated and solvated state, is positive, intercalation of desolvated anions into MXene sheets is more feasible due to less positive free energy. Experimental considerations such as pre-intercalation of IL into the MXene sheets and the complex electrode formulation may bring some level of heterogeneity to the electrode architecture, which were not taken into consideration by the DFT calculations. These factors could have profound influence on anion intercalation into MXene sheets, possibly contributing to charge storage capacity via anion pseudo-intercalation. Therefore, cation and anion intercalation are more feasible in the desolvated state. The intercalants, $EMIM^+$ and $TFSI^-$ do not need a solvation shell for proficient intercalation as they are solvent-free electrolyte systems.[43] However, under non-equilibrium (extreme potentials) conditions, anion intercalation may occur provided that electrode | electrolyte interface is electrochemically stable. Anion pseudo-intercalation charge storage mechanism was demonstrated in lanthanum based perovskite electrode materials where oxygen vacancy mediated redox capacitance was observed.[44] In the case of graphitic carbon materials, intercalation of anions was observed at anodic potentials > 4.5 vs. Li/Li^+, where staging intercalation process was demonstrated.[45] High potentials and surface chemistry modifications of MXenes may be necessary to facilitate the anion intercalation in MXene electrodes.

This study suggests a possibility of anion pseudo-intercalation into MXene interlayer space. However, to achieve mechanistic understanding of the process and unambiguously determine the origin of the peaks in CVs, the use of advanced techniques, such as electrochemical quartz crystal microbalance (EQCM), in-situ diffraction, and spectroscopic studies, will be needed. Exploring MXene in concentrated or solvent-free electrolytes may lead to the development of high-power, high-energy storage devices employing MXenes. Given the compositional versatility of MXenes and ILs, the right electrode | electrolyte combination must be found before embarking on experimental investigations. Such studies could advance the understanding of MXene based materials as charge hosts for developing energy storage devices.

Conclusion

Ionic liquid pre-intercalated small (~150 nm) flakes of $Ti_3C_2T_x$ were employed to produce an ionically conductive active layer on a compact, thin, and electronically conducting $Ti_3C_2T_x$ current collector producing an all-MXene electrode. Investigation of electrochemical performance of these electrodes in ionic liquid electrolyte showed a wide capacitive envelop and expansion of the electrochemical stability window to about 2.7 V. Electrochemical signatures at about −0.75 V and +0.75 V (vs. Ag wire) suggest a possibility of ambipolar electrochemistry, signifying adsorption/intercalation of anions and cations from 1-ethyl-3-methylimidazolium bis-(trifluoromethylsulfonyl)-imide (EMIM-TFSI) between nanometer-thin $Ti_3C_2T_x$ sheets. Electrochemical impedance analysis revealed sluggish diffusion kinetics of anions over cations across $Ti_3C_2T_x$ galleries. Density functional theory calculations suggest that the cation intercalates into the MXene interlayer space occurs spontaneously, while only desolvated anions may be intercalated. This study provides a pathway for exploring anion pseudo-intercalation across specific MXene compositions in concentrated electrolytes and may lead to development of improved energy storage devices.

Experimental Section

All chemicals were used as received, without further purification. Layered ternary carbide Ti_3AlC_2 (MAX phase, < 40 μm particle size) powder was synthesized as previously reported.[29]

Synthesis of delaminated $Ti_3C_2T_x$ MXene (d-$Ti_3C_2T_x$). Minimal amount of hydrofluoric acid (HF), ca. 5 wt.%, was used in etching Ti_3AlC_2 MAX phase.[46] The etching recipe was comprised of 12 mL concentrated hydrochloric acid (HCl, Fisher, technical grade, 35%–38%), 6 mL deionized water and 2 mL of concentrated hydrofluoric acid (HF, 49%). While stirring at 300 rpm, 1 g of Ti_3AlC_2 powder was slowly added into the vial and the stirring was continued for 24 h at 35 °C. After etching reaction, washing was done with deionized (DI) water via centrifugation for 5 minutes at 3500 rpm for several times. Colorless acidic supernatant was decanted after each washing step until reaching neutral pH. The wet slurry of multilayer $Ti_3C_2T_x$ MXene was added into a solution of 1 g lithium chloride (LiCl, Alfa Aesar, 98 + %) in 50 mL of DI water followed by manual shaking for 5 minutes.[47] Hydrated Li-ions get intercalated into $Ti_3C_2T_x$ sheets and the solution was stirred for 24 h at 35 °C. The produced suspension was washed with DI water and centrifuged to decant clear supernatant until pH ≥ 6 was reached. A stable dark green supernatant of $Ti_3C_2T_x$ was collected after 30 min centrifugation at 3500 rpm. The concentration of $Ti_3C_2T_x$ colloidal suspension was measured by filtering the solution through a polypropylene filter (3501 Coated PP, Celgard LLC), followed by drying under vacuum at 70 °C overnight.

$Ti_3C_2T_x$ free-standing films preparation. Large area freestanding $Ti_3C_2T_x$ films were prepared by a blade coating method that was reported in our previous work.[30] In our study, highly concentrated $Ti_3C_2T_x$ dispersions (48 mg/mL) containing predominantly large MXene flakes was used to get highly conductive $Ti_3C_2T_x$ films. The height between the substrate and the blade edge has been adjusted to 75 μm, 100 μm, and 200 μm which corresponds to dry film thickness of 7 μm, 10 μm, and 20 μm, respectively.

Batteries & Supercaps

Research Article
doi.org/10.1002/batt.202300009

Chemistry
Europe
European Chemical
Societies Publishing

Small flake slurry coating. To obtain $Ti_3C_2T_x$ MXene of smaller flake size, large flake $Ti_3C_2T_x$ dispersion was sonicated for 45 minutes using a probe sonicator (Fisher Scientific model 505 Sonic Dismembrator, 500 W) with 8 s ON pulse and a 2 s OFF pulse at an amplitude of 50% in an ice bath. The resulting small flake MXene dispersion in water was filtered by vacuum assisted filtration to remove water. While it was still wet, further solvent exchange was done by vacuum filtering propylene carbonate (PC, Sigma Aldrich) (for 40 mg of MXene, we used 3 mL of PC) followed by 1-ethyl-3-methylimidazolium bis(trifluoromethylsulfonyl)imide (EMIM-TFSI) neat IL through the $Ti_3C_2T_x$ wet filtrate cake. Thus, obtained pre-intercalated MXene film was ground in a mortar and dried under vacuum at 120 °C overnight to get rid of PC. Due to non-volatile nature of IL, wet state of pre-intercalated MXene was used as an active electrode material (80 wt%). 10 wt% of conductive carbon (Super P C645, Timical) and 10 wt% of polyvinylidene fluoride (PVDF, Sigma Aldrich) binder were added with minimal amount of N-methyl-2-pyrrolodine (NMP) to make a slurry. Doctor blade casting was employed to spread the slurry on top of MXene current collector film. These wet films were dried under vacuum at 80 °C for 12 h followed by densification with a 1 kg cylinder rolling over it (corresponds to 2 kg/cm²).

Material characterization. Structure of $Ti_3C_2T_x$ and IL pre-intercalated $Ti_3C_2T_x$ was investigated by X-ray diffraction (XRD) using Rigaku Smart Lab (Tokyo, Japan) diffractometer with Cu K_α radiation (voltage and current settings were 40 kV and 44 mA, respectively) with a step scan of 0.04°, 2θ range 3°–50° and dwell time of 0.5 s. $Ti_3C_2T_x$ MXene flake size was determined by employing dynamic light scattering (DLS, Zetasizer Nano ZS, Malvern Instruments, USA). Five measurements were taken for each sample and the average value was reported. The morphology of the $Ti_3C_2T_x$ MXene was imaged using a scanning electron microscope (SEM) (Zeiss Supra 50VP, Germany). Thickness of the casted IL pre-intercalated $Ti_3C_2T_x$ was estimated using cross-sectional SEM. The electrical conductivity of $Ti_3C_2T_x$ samples was determined using a four-point probe conductivity meter (ResTest v1, Jandel Engineering Ltd., Bedfordshire, UK) with a probe distance of 1 mm (applied current was 0.5 mA).

Activated carbon (AC) films. Activated carbon (AC, YP50F grade) films were prepared by mixing 5 wt% polytetrafluoroethylene (60 wt% in water, Sigma Aldrich) and 95 wt% of YP50F (Kuraray, Japan). The above slurry was rolled into ~100 μm thick films followed by drying in a vacuum oven at 70 °C for 12 h. These AC films were used as over-capacitive counter electrode for the 3-electrode measurements.

Electrochemical measurements. Cyclic voltammetry (CV), galvanostatic charge-discharge (GCD), and electrochemical impedance spectroscopy (EIS) were conducted at room temperature (RT) using a VMP3 electrochemical workstation (BioLogic, France). CVs were recorded at different scan rates (1–100 mV/s) in the potential window of −1.5 to 1.0 V (vs. Ag wire). The 3-electrode measurements were performed in neat EMI-TFSI and 1 M EMI-TFSI in propylene carbonate (PC) electrolytes. $Ti_3C_2T_x$ electrodes with pre-intercalated IL (areal mass loading of 2.0 mg/cm^{-2}) were employed as the working electrode with over-capacitive AC film and Ag wire (1 mm diameter) as the counter and reference electrodes, respectively.

Gravimetric specific capacitance C_m (F/g) of electrode materials was calculated from the CV curves by integrating the discharge portion using the following equation:

$$C_m = \frac{1}{Vmv} \int i\,dV \tag{2}$$

where i is the current (mA), V is the potential window (V), $\boldsymbol{v}$ is the scan rate (mV/s) and m is the mass (mg) of the active material contributing to the acquired charge storage.

Volumetric capacitance was estimated by multiplying gravimetric capacitance with the density of the electrodes.

$$C_V = C_m \times \text{density} \tag{3}$$

The real part of capacitance (C') over the frequency range was estimated by approximating $Ti_3C_2T_x$ MXene | electrolyte interface with an equivalent circuit model having a simple resistor and capacitor in series in the frequency range of 10 mHz to 10 Hz.[48] C' values were derived from the impedance analysis of MXene electrodes in different electrolytes. The real capacitance, C' and imaginary capacitance, C'' were calculated according to the following equations:

$$C' = -Z''/2\pi f|Z|^2 \tag{4}$$

$$C'' = Z'/2\pi f|Z|^2 \tag{5}$$

where $|Z|$ is the absolute value of impedance (Ω), Z' and Z'' are the real and imaginary components of impedance, respectively, and f is the frequency (Hz).[39]

Phase angle ($\emptyset$) is given by the following expression

$$\emptyset = -\tan^{-1}\frac{Z'(\omega)}{Z''(\omega)} \tag{6}$$

Warburg coefficient (σ) is estimated from the slope of Z' vs. $\omega^{-1/2}$ ($Z' = \sigma \ \omega^{-1/2}$) and it is inversely proportional to the diffusion coefficient ($D \sim \sigma^{-2}$).[40]

Staircase potentio-electrochemical impedance spectroscopy (SPEIS). SPEIS is a powerful technique that uses successive impedance measurements at different potentials to investigate the electrode kinetics. SPEIS measurements were done by applying step potential intervals of 25 mV with an AC amplitude of 10 mV to $Ti_3C_2T_x$ MXene electrodes in the frequency range of 10 mHz–100 kHz with six points per decade in logarithmic spacing within the same voltage window as cyclic voltammetry.[49] During SPEIS measurements, a preconditioning step (chronoamperometry) was applied at the selected potentials for 10 minutes before collecting the impedance data to ensure equilibrium conditions at each step. Low frequency data spanning from 10 mHz to 10 Hz was considered for constructing 3D Bode maps of capacitance (C' and C'')-frequency-potential and phase angle-frequency-potential along XYZ axes.

Computational methods. Density functional theory (DFT)-based theoretical calculations were performed using a plane-wave basis set implemented in Vienna Ab initio Simulation Package (VASP).[50] The project augmented wave (PAW) potentials were used for all elements to describe the interaction between valence and core electrons.[51] The exchange-correlation energy term is calculated by generalized gradient approximation (GGA) described by Perdew-Burke-Ernzerhof (PBE).[52] To explain van der Waals (vdW) correction, DFT–D3 method of Grimme was used.[53] The geometry optimization was done using the conjugate gradient algorithm.[54] For better geometry, the kinetic energy cut-off for the plane-wave basis set was set to 520 eV. During relaxation of the structure, the convergence criteria for energy and force between two self-consistent steps were smaller than 10^{-5} eV and 0.01 eV/Å, respectively. The integrations in the k-space were performed by sampling the Brillouin zone using a $3\times3\times1$ Monkhorts-Pack

Batteries & Supercaps

Research Article
doi.org/10.1002/batt.202300009

Chemistry
Europe

European Chemical
Societies Publishing

scheme with the smallest spacing of 0.03 Å⁻¹ between k-points.[55] We were allowed to relax ionic positions throughout the calculation by fixing the cell shape and volume. We initiated our optimization with a unit cell of MXene sheet having formula $Ti_3C_3O_2$; the lattice parameters for this structure are taken from the literature.[56] From the optimized structure, a supercell of $4 \times 4 \times 1$ of given stoichiometry $Ti_3C_2O_{0.84}F_{0.25}(OH)_{0.06}$ was constructed to study the intercalation chemistry of cation and anion in the MXene interlayer space.[25] All the calculations were performed considering this stoichiometry. The optimized structures were visualized using VESTA software.[57] Solvent was treated as self-consistent continuum model where the microscopic interactions were generalized using common physical properties.

Conflict of Interest

The authors declare no conflict of interest.

Data Availability Statement

The data that support the findings of this study are available in the supplementary material of this article. Original data are available from the authors on a reasonable request.

[1] P. Ratajczak, M. E. Suss, F. Kaasik, F. Béguin, *Energy Storage Mater.* **2019**, *16*, 126–145.

[2] P. Simon, Y. Gogotsi, *Nat. Mater.* **2020**, *19*, 1151–1163.

[3] S. Fleischmann, Y. Zhang, X. Wang, P. T. Cummings, J. Wu, P. Simon, Y. Gogotsi, V. Presser, V. Augustyn, *Nat. Energy* **2022**, *7*, 222–228.

[4] X. Wang, M. Salari, D.-e. Jiang, J. Chapman Varela, B. Anasori, D. J. Wesolowski, S. Dai, M. W. Grinstaff, Y. Gogotsi, *Nat. Rev. Mater.* **2020**, *5*, 787–808.

[5] M. Naguib, M. Kurtoglu, V. Presser, J. Lu, J. Niu, M. Heon, L. Hultman, Y. Gogotsi, M. W. Barsoum, *Adv. Mater.* **2011**, *23*, 4248–4253.

[6] J. Nan, X. Guo, J. Xiao, X. Li, W. Chen, W. Wu, H. Liu, Y. Wang, M. Wu, G. Wang, *Small* **2021**, *17*, 1902085.

[7] J. Pang, R. G. Mendes, A. Bachmatiuk, L. Zhao, H. Q. Ta, T. Gemming, H. Liu, Z. Liu, M. H. Rummeli, *Chem. Soc. Rev.* **2019**, *48*, 72–133.

[8] M. R. Lukatskaya, S. Kota, Z. Lin, M.-Q. Zhao, N. Shpigel, M. D. Levi, J. Halim, P.-L. Taberna, M. W. Barsoum, P. Simon, Y. Gogotsi, *Nat. Energy* **2017**, *2*, 17105.

[9] Q. Jiang, N. Kurra, M. Alhabeb, Y. Gogotsi, H. N. Alshareef, *Adv. Energy Mater.* **2018**, *8*, 1703043.

[10] B. Anasori, M. R. Lukatskaya, Y. Gogotsi, *Nat. Rev. Mater.* **2017**, *2*, 16098.

[11] F. Ming, H. Liang, G. Huang, Z. Bayhan, H. N. Alshareef, *Adv. Mater.* **2020**, *33*, 2004039.

[12] M. Okubo, A. Sugahara, S. Kajiyama, A. Yamada, *Acc. Chem. Res.* **2018**, *51*, 591–599.

[13] K. R. G. Lim, M. Shekhirev, B. C. Wyatt, B. Anasori, Y. Gogotsi, Z. W. Seh, *Nat. Synthesis* **2022**, *1*, 601–614.

[14] M. R. Lukatskaya, O. Mashtalir, C. E. Ren, Y. Dall'Agnese, P. Rozier, P. L. Taberna, M. Naguib, P. Simon, M. W. Barsoum, Y. Gogotsi, *Science* **2013**, *341*, 1502–1505.

[15] J. Tang, T. S. Mathis, N. Kurra, A. Sarycheva, X. Xiao, M. N. Hedhili, Q. Jiang, H. N. Alshareef, B. Xu, F. Pan, Y. Gogotsi, *Angew. Chem. Int. Ed.* **2019**, *58*, 17849–17855.

[16] M. B. Miltenburg, S. Y. An, N. K. Obhi, E. Grignon, B. T. McAllister, D. S. Seferos, *ACS Appl. Polym. Mater.* **2020**, *2*, 5574.

[17] Z. Lin, H. Shao, K. Xu, P.-L. Taberna, P. Simon, *Trends Chem.* **2020**, *2*, 654–664.

[18] J. Luo, W. Zhang, H. Yuan, C. Jin, L. Zhang, H. Huang, C. Liang, Y. Xia, J. Zhang, Y. Gan, X. Tao, *ACS Nano* **2017**, *11*, 2459–2469.

[19] Y. Dall'Agnese, P. Rozier, P.-L. Taberna, Y. Gogotsi, P. Simon, *J. Power Sources* **2016**, *306*, 510–515.

[20] K. Liang, R. A. Matsumoto, W. Zhao, N. C. Osti, I. Popov, B. P. Thapaliya, S. Fleischmann, S. Misra, K. Prenger, M. Tyagi, E. Mamontov, V. Augustyn, R. R. Unocic, A. P. Sokolov, S. Dai, P. T. Cummings, M. Naguib, *Adv. Funct. Mater.* **2021**, *31*, 2104007.

[21] M.-Q. Zhao, C. E. Ren, Z. Ling, M. R. Lukatskaya, C. Zhang, K. L. Van Aken, M. W. Barsoum, Y. Gogotsi, *Adv. Mater.* **2015**, *27*, 339–345.

[22] J. Yan, C. E. Ren, K. Maleski, C. B. Hatter, B. Anasori, P. Urbankowski, A. Sarycheva, Y. Gogotsi, *Adv. Funct. Mater.* **2017**, *27*, 1701264.

[23] X. Wang, T. S. Mathis, K. Li, Z. Lin, L. Vlcek, T. Torita, N. C. Osti, C. Hatter, P. Urbankowski, A. Sarycheva, M. Tyagi, E. Mamontov, P. Simon, Y. Gogotsi, *Nat. Energy* **2019**, *4*, 241–248.

[24] X. Wang, T. S. Mathis, Y. Sun, W.-Y. Tsai, N. Shpigel, H. Shao, D. Zhang, K. Hantanasirisakul, F. Malchik, N. Balke, D.-e. Jiang, P. Simon, Y. Gogotsi, *ACS Nano* **2021**, *15*, 15274–15284.

[25] N. Shpigel, A. Chakraborty, F. Malchik, G. Bergman, A. Nimkar, B. Gavriel, M. Turgeman, C. N. Hong, M. R. Lukatskaya, M. D. Levi, Y. Gogotsi, D. T. Major, D. Aurbach, *J. Am. Chem. Soc.* **2021**, *143*, 12552–12559.

[26] A. K. Tomar, T. Kshetri, N. H. Kim, J. H. Lee, *Energy Storage Mater.* **2022**, *50*, 86–95.

[27] Z. Lin, D. Barbara, P.-L. Taberna, K. L. Van Aken, B. Anasori, Y. Gogotsi, P. Simon, *J. Power Sources* **2016**, *326*, 575–579.

[28] Z. Lin, P. Rozier, B. Duployer, P.-L. Taberna, B. Anasori, Y. Gogotsi, P. Simon, *Electrochem. Commun.* **2016**, *72*, 50–53.

[29] T. S. Mathis, K. Maleski, A. Goad, A. Sarycheva, M. Anayee, A. C. Foucher, K. Hantanasirisakul, C. E. Shuck, E. A. Stach, Y. Gogotsi, *ACS Nano* **2021**, *15*, 6420–6429.

[30] J. Zhang, N. Kong, S. Uzun, A. Levitt, S. Seyedin, P. A. Lynch, S. Qin, M. Han, W. Yang, J. Liu, X. Wang, Y. Gogotsi, J. M. Razal, *Adv. Mater.* **2020**, *32*, 2001093.

[31] X. Qi, B. Blizanac, A. DuPasquier, P. Meister, T. Placke, M. Oljaca, J. Li, M. Winter, *Phys. Chem. Chem. Phys.* **2014**, *16*, 25306–25313.

[32] Q. Jiang, N. Kurra, K. Maleski, Y. Lei, H. Liang, Y. Zhang, Y. Gogotsi, H. N. Alshareef, *Adv. Energy Mater.* **2019**, *9*, 1901061.

[33] X. Yao, Y. Zhao, F. A. Castro, L. Mai, *ACS Energy Lett.* **2019**, *4*, 771–778.

[34] N. Jäckel, B. Krüner, K. L. Van Aken, M. Alhabeb, B. Anasori, F. Kaasik, Y. Gogotsi, V. Presser, *ACS Appl. Mater. Interfaces* **2016**, *8*, 32089.

[35] J. Wang, J. Polleux, J. Lim, B. Dunn, *J. Phys. Chem. C* **2007**, *111*, 14925–14931.

[36] T. S. Mathis, N. Kurra, X. Wang, D. Pinto, P. Simon, Y. Gogotsi, *Adv. Energy Mater.* **2019**, *9*, 1902007.

[37] K. Xu, C. Merlet, Z. Lin, H. Shao, P.-L. Taberna, L. Miao, J. Jiang, J. Zhu, P. Simon, *Energy Storage Mater.* **2020**, *33*, 460–469.

[38] S. Wang, J. Zhang, O. Gharbi, V. Vivier, M. Gao, M. E. Orazem, *Nat. Rev. Methods Primers* **2021**, *1*, 41.

Batteries & Supercaps

Research Article
doi.org/10.1002/batt.202300009

Chemistry Europe
European Chemical
Societies Publishing

[39] P. L. Taberna, P. Simon, J. F. Fauvarque, *J. Electrochem. Soc.* **2003**, *150*, A292.

[40] M. D. Levi, D. Aurbach, *Electrochim. Acta* **1999**, *45*, 167–185.

[41] K. Mathew, V. S. C. Kolluru, S. Mula, S. N. Steinmann, R. G. Hennig, *J. Chem. Phys.* **2019**, *151*, 234101.

[42] K. Mathew, R. Sundararaman, K. Letchworth-Weaver, T. A. Arias, R. G. Hennig, *J. Chem. Phys.* **2014**, *140*, 084106.

[43] C. Arbizzani, M. Biso, D. Cericola, M. Lazzari, F. Soavi, M. Mastragostino, *J. Power Sources* **2008**, *185*, 1575.

[44] J. T. Mefford, W. G. Hardin, S. Dai, K. P. Johnston, K. J. Stevenson, *Nat. Mater.* **2014**, *13*, 726–732.

[45] M. Zhang, X. Song, X. Ou, Y. Tang, *Energy Storage Mater.* **2019**, *16*, 65–84.

[46] M. Alhabeb, K. Maleski, B. Anasori, P. Lelyukh, L. Clark, S. Sin, Y. Gogotsi, *Chem. Mater.* **2017**, *29*, 7633–7644.

[47] A. Sarycheva, A. Polemi, Y. Liu, K. Dandekar, B. Anasori, Y. Gogotsi, *Sci. Adv.* **2018**, *4*, eaau0920.

[48] N. Kurra, S. Uzun, G. Valurouthu, Y. Gogotsi, *Energy Storage Mater.* **2021**, *39*, 347–353.

[49] J. S. Ko, C.-H. Lai, J. W. Long, D. R. Rolison, B. Dunn, J. Nelson Weker, *ACS Appl. Mater. Interfaces* **2020**, *12*, 14071–14078.

[50] G. Kresse, J. Furthmüller, *Phys. Rev. B* **1996**, *54*, 11169–11186.

[51] P. E. Blöchl, *Phys. Rev. B* **1994**, *50*, 17953–17979.

[52] J. P. Perdew, K. Burke, M. Ernzerhof, *Phys. Rev. Lett.* **1996**, *77*, 3865–3868.

[53] S. Grimme, J. Antony, S. Ehrlich, H. Krieg, *J. Chem. Phys.* **2010**, *132*, 154104.

[54] G. Yuan, T. Li, W. Hu, *J. Inequal. Appl.* **2019**, *2019*, 247.

[55] H. J. Monkhorst, J. D. Pack, *Phys. Rev. B* **1976**, *13*, 5188–5192.

[56] T. Hu, J. Wang, H. Zhang, Z. Li, M. Hu, X. Wang, *Phy. Chem. Chem. Phys.* **2015**, *17*, 9997–10003.

[57] K. Momma, F. Izumi, *J. Appl. Crystallogr.* **2008**, *41*, 653–658.